Indium Gallium Arsenide/Gallium Arsenide Antimonide Type II Superlattice Photodetector That Can Utilize Night Airglow

Masatoshi Koyama,[1*] Junichi Kudo,[1] Yasuhiro Iguchi,[2] Hiroshi Inada,[2]
Yasuhiro Muramatsu,[3*] Isamu Kumihashi,[3] and Masahiro Sano[3]

[1]Future Capabilities Development Center, Acquisition Technology & Logistics Agency, Ministry of Defense,
1-2-24, Ikejiri, Setagaya-ku, Tokyo 154-8511, Japan
[2]Sumitomo Electric Industries, Ltd., 1, Taya-cho, Sakae-ku, Yokohama, Kanagawa 244-8588, Japan
[3]NEC Corporation, 1-10, Nisshin-cho, Fuchu-shi, Tokyo 183-8501, Japan

Since 2016, we have worked on the development of short-wavelength infrared (SWIR) type II superlattice (T2SL) photodetectors that can utilize night airglow. In addition to the normal SWIR band, the photodetector can detect wavelengths longer than 1.7 μm, which indium gallium arsenide sensors cannot detect, and can effectively utilize illumination by atmospheric phenomena, often called night airglow. To confirm its technical feasibility, we fabricated T2SL single-pixel pin-photodiode experimental samples based on the results of T2SL structural simulation. Using these samples, we obtained various data such as dark current density and spectral sensitivity. On the basis of the data, we considered the appropriate structural parameters and operating conditions of the SWIR T2SL photodetector. Finally, we fabricated a focal plane array with 640 × 512 pixels and confirmed that the photodetector can obtain clear images.

1. Introduction

The conventionally used mid-wavelength infrared and long-wavelength infrared sensors are thermal sensors that detect infrared rays emitted from all objects warmer than absolute zero temperature, and they are very useful in searching for heat sources when the target is warmer than the background. In contrast to thermal sensors, such as visible sensors, short-wavelength infrared (SWIR) sensors detect the reflection or absorption of photons at the surface of the target; thus, SWIR images often have a higher contrast than thermal images, making it easier to identify various objects. Also, SWIR sensors can distinguish colors that are visually indistinguishable.[1] Moreover, SWIR has a longer wavelength than visible light and is less affected by fine particles in the atmosphere. By taking advantage of these characteristics, SWIR sensors are used in various applications such as inspection, quality control, identification, sorting, and surveillance.

Most recently, significant advances in the development of indium gallium arsenide (InGaAs) sensors have made it possible to practically detect wavelengths between 0.9 and 1.7 μm in SWIR. Since InGaAs sensors do not require a large and heavy mechanical cooler, they are compact and lightweight and have low power consumption. Also, unlike night-vision goggles using an image intensifier, the image is digitized, so the images can be sent to remote locations or appropriate image processing can be applied as needed. In addition, InGaAs sensors can detect illumination by atmospheric phenomena, called night sky radiance (often called night airglow) mostly at SWIR. Thus, if there is a high-performance SWIR sensor that can detect wavelengths longer than 1.7 μm, night airglow can be utilized more efficiently. This means that nighttime surveillance can be easier and more effective than ever before. Also, by using a SWIR band laser with a wavelength longer than 1.7 μm, targets can be sighted and illuminated at wavelengths that cannot be detected by InGaAs sensors.

In addition to InGaAs sensors, there are mercury cadmium telluride (HgCdTe) and indium antimonide sensors that can detect SWIR. However, to use them with practical signal-to-noise ratios, they must be cooled to extremely low temperatures with a large and heavy mechanical cooler. HgCdTe also requires mercury as a material, which is restricted worldwide because it causes environmental pollution and health hazards.

In recent years, many research studies have been conducted on the type II superlattice (T2SL), which is capable of achieving both a longer detection wavelength band and a lower dark current, which cannot be achieved with ordinary bulk semiconductors. Unlike HgCdTe, T2SL has the advantage of not requiring mercury as a material. Thus, InGaAs/GaAsSb (gallium arsenide antimonide) T2SL sensors have been proposed as sensors capable of detecting 2 μm band SWIR.[2,3] Therefore, we decided to work on realizing an InGaAs/GaAsSb-based T2SL photodetector that can utilize night airglow.

2. T2SL Structural Simulation

2.1 Target of detection wavelength band

Night airglow in the SWIR band is mainly composed of emission lines from OH radical molecules in the light-emitting layer. As shown in Fig. 1, during the day, UV photons from the sun cause water molecules to decompose into hydrogen and ozone molecules in the upper atmosphere of the earth. At night, OH molecules in an excited state are generated by the recombination of these molecules. After that, the molecules transition to a lower energy state and emit a SWIR photon.[4]

Also, the wavelength bands of night airglow are approximately 0.6 to 2.2 μm and 2.8 to 4.5 μm.[5] However, in observations from the ground, the effect of atmospheric thermal radiation becomes stronger at wavelengths above 2.3 μm; thus, we set the wavelength of night airglow to 0.6–2.2 μm.

In addition, the lower the operating temperature and the shorter the cutoff wavelength, the lower the dark current density.[6] Therefore, it is desirable that the cutoff wavelength is longer than 2.2 μm and as close to 2.2 μm as possible.
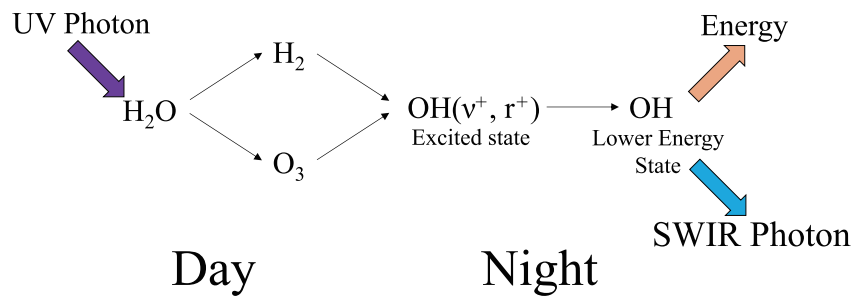
Fig. 1.   (Color online) Synoptic sketch of the occurrence of night airglow.

2.2   T2SL structural parameter simulation

Figure 2 shows the band structure of the InGaAs/GaAsSb T2SL. Light absorption occurs in the overlapping part of the wave function of electrons confined in the quantum well in the conduction band of InGaAs and the wave function of holes confined in the quantum well in the valence band of GaAsSb. The detection wavelength band corresponds to the energy difference between the ground states of electrons and holes in the T2SL structure. The detection wavelength band can also be adjusted by changing the thickness of each layer. Moreover, the detection sensitivity is considered to be proportional to the transition probability from the ground state of holes to the ground state of electrons, and the transition probability is proportional to the square of the overlap between the electron wave function and the hole wave function.[7] To calculate the detection wavelength band and overlap of the wave functions, it is necessary to obtain the wave functions and energy eigenvalues of the ground states of electrons and holes for the superlattice structure, and these can be calculated by solving the Schrödinger equation. Although the actual superlattice structure is three-dimensional, it is almost uniform in the in-plane direction (crystal growth direction and its perpendicular direction) of the substrate. The three-dimensional Schrödinger equation can be separated into variables, resulting in solving the one-dimensional Schrödinger equation in the crystal growth direction.

It is worth noting that we selected indium phosphide (InP) as the T2SL crystal growth substrate. InP substrates have an average transmittance of about 70% in the 0.9–12 μm band.[8] In contrast, the GaSb substrate typically used in mid-wavelength infrared T2SL does not transmit wavelengths below 1.6 μm, and the average transmittance is approximately 30% even at wavelengths of 1.6 to 5.0 μm.[9] Therefore, even if a small amount of the GaSb substrate remains, the transmittance in the SWIR band will decrease significantly, so an extremely advanced technology is required to completely remove the GaSb substrate. Then, both InGaAs and GaAsSb are lattice-matched to the InP substrate, and it is possible to suppress crystal defects due to the lattice mismatch and reduce the dark current. Moreover, InP substrates are manufactured by domestic manufacturers and are widely available in Japan. From these characteristics, we selected InP as the crystal growth substrate.

In this study, we numerically solved the one-dimensional Schrödinger equation in a superlattice structure using COMSOL Multiphysics 5.3. The "coefficient form PDE", which is a
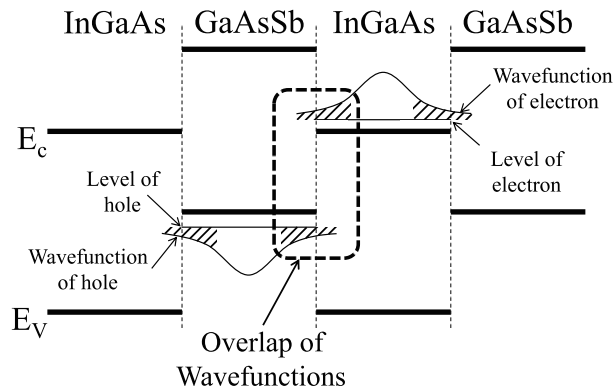
Fig. 2.   Band structure of the InGaAs/GaAsSb superlattice.

model for solving partial differential equations, was used as the analytical model. The geometry used for the calculation is InP/(InGaAs/GaAsSb T2SL 20 pairs)/InP, because we assume a structure in which a superlattice grown on an InP substrate is covered with an InP cap layer. A schematic diagram of the geometry used is shown in Fig. 3.

In this geometry, considering that the effective masses of electrons and holes and the energies of the conduction and valence band edges are different for each semiconductor composition, the one-dimensional Schrödinger equations to be solved are expressed by Eqs. (1) and (2).

$$-\frac{d}{dx}\left(\frac{\hbar^2}{2m_e(x)m_0}\frac{d}{dx}\psi_e(x)\right)+V_e(x)\psi_e(x)=E_e\psi_e(x) \tag{1}$$

$$-\frac{d}{dx}\left(\frac{\hbar^2}{2m_h(x)m_0}\frac{d}{dx}\psi_h(x)\right)+V_h(x)\psi_h(x)=E_h\psi_h(x) \tag{2}$$

Note that m_e is the effective mass of electrons, m_h is the effective mass of holes, V_e is the energy of the conduction band edge, V_h is the energy of the valence band edge, E_e is the electron energy eigenvalue, E_h is the hole energy eigenvalue, Ψ_e is the electron wave function, and Ψ_h is the hole wave function. As shown in Fig. 3, the left and right ends of the geometry are terminated with wide-gap InP, so we assumed that the wave functions of both electrons and holes are sufficiently attenuated at both ends of the analytical space. Therefore, we set a Neumann-type boundary condition in which the differential coefficient of the wave function at both ends of the geometry is 0. Also, since conventional SWIR sensors generally operate at room temperature, we performed simulations at an operating temperature of 300 K in this study.

Next, the overlap S between the electron and hole wave functions is obtained by numerical integration over the entire analytic space according to Eq. (3). Here, * means the complex conjugate.
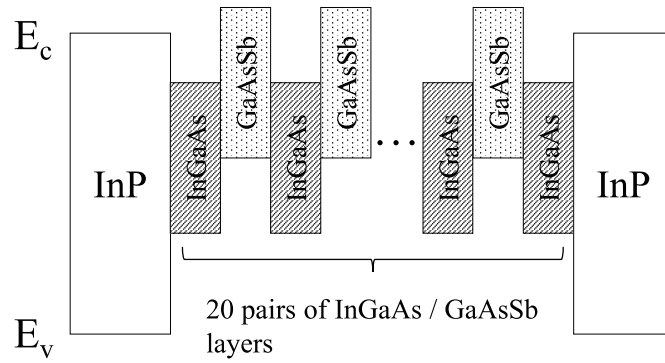
Fig. 3.   Schematic diagram of the superlattice structure used in the simulations.

$$S = \int \psi_e^*(x) \psi_h(x) dx \tag{3}$$

2.3   Cutoff wavelength in T2SL structural parameter simulation

As described in Sect. 2.1, it is desirable that the cutoff wavelength is longer than 2.2 μm and as close to 2.2 μm as possible; also, the lower the operating temperature, the lower the dark current density. In addition, on the basis of the results of a similar measurement that we conducted in 2015, the sensitivity around the 2.2 μm band deteriorates when the operating temperature is lower than about 170 K. Therefore, in this study, the operating temperature is assumed to be approximately 170 K.

Figure 4 shows the relationship between the cutoff wavelength and the operating temperature obtained from a similar measurement in 2015. Within the measured range of 150 to 298 K, the higher the operating temperature, the longer the cutoff wavelength. Assuming that the cutoff wavelength at temperature T (K) is $\lambda_{CO}(T)$ (μm), the equation below is obtained.

$$\lambda_{CO} = \frac{hc}{E_g(T)} = \frac{1.24}{E_g(T)} \tag{4}$$

Here, h is Planck's constant [6.63×10^{-34} (J・s), 4.14×10^{-15} (eV・s)], c is the speed of light [3.0×10^8 (m・sec^{-1})], and $E_g(T)$ (eV) is the energy gap at the temperature T (K) of the material of the photodetector.

On the other hand, there is a relationship between the energy gap of the semiconductor and the operating temperature of the photodetector as shown in Eq. (5) as Varshni's empirical equation.[10]
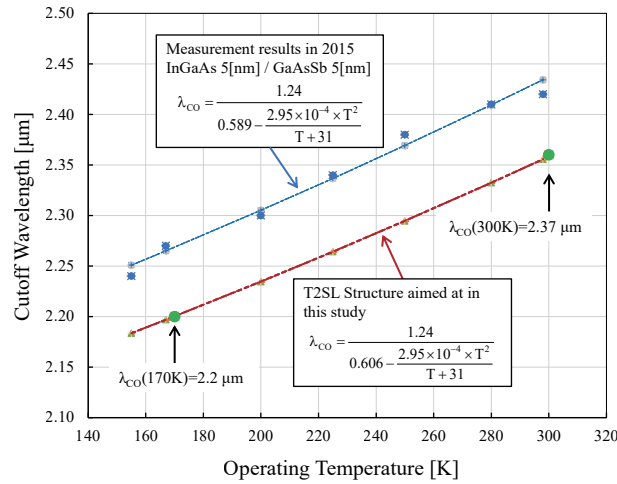
$$E_g(T) = E_g(0) - \frac{\alpha T^2}{T + \beta} \tag{5}$$

Fig. 4.   (Color online) Relationship between the cutoff wavelength and the operating temperature.

Then, α and β are constants that depend on the material of the photodetector. The reference shows that Eq. (5) can be applied to superlattices as well.[11] Therefore, we attempted to fit the results of the similar measurement in 2015 using Eq. (5), and we were able to obtain good agreement as shown by the broken line in Fig. 5 in the following cases:

$$\alpha = 3.07 \times 10^{-4}\ (\text{eV} \cdot \text{K}^{-1}),$$
$$\beta = 32\ (\text{K}),$$
$$E_g(0) = 0.589\ (\text{eV}).$$

That is, the temperature dependences of the energy gap and cutoff wavelength of the InGaAs:5 nm/GaAsSb:5 nm SWIR photodetector measured in 2015 are expressed by Eqs. (6) and (7), respectively.

$$E_g\left(T\right) = 0.589 - \frac{3.07 \times 10^{-4} \times T^2}{T + 32} \tag{6}$$

$$\lambda_{CO}\left(T\right) = 0.589 - \frac{1.24}{0.589 - \dfrac{3.07 \times 10^{-4} \times T^2}{T + 32}} \tag{7}$$

The materials of the photodetector are the same as those used in the measurement in 2015. Therefore, from Eqs. (6) and (7), when $T = 170$ K, we calculate $E_g(0)$, where λ_{co} is 2.2 μm. As a result, the temperature dependence of the energy gap and cutoff wavelength of the SWIR T2SL photodetector are expressed by Eqs. (8) and (9), respectively.

$$E_g\left(T\right) = 0.608 - \frac{3.07 \times 10^{-4} \times T^2}{T + 32} \tag{8}$$
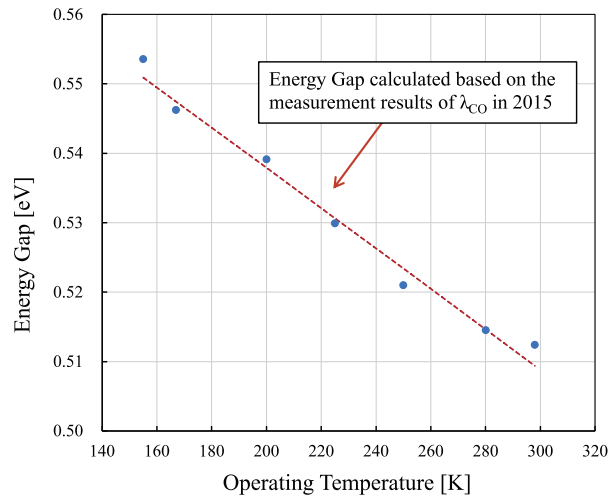
Fig. 5.　(Color online) Operating temperature dependence of the energy gap of the InGaAs/GaAsSb-based devices.

$$\lambda_{CO}(T) = 0.608 - \frac{1.24}{0.608 - \dfrac{3.07 \times 10^{-4} \times T^2}{T + 32}} \tag{9}$$

From the above, the T2SL structure that satisfies the cutoff wavelength of 2.2 μm at the operating temperature of 170 K corresponds to a T2SL structure with a cutoff wavelength of 2.37 μm in the T2SL structural simulation performed at the operating temperature of 300 K.

2.4　Results of T2SL structural simulation

Figure 6 shows the simulation results of the relationship between the thicknesses of the InGaAs/GaAsSb layers and the cutoff wavelength when the operating temperature is 300 K. On the basis of Fig. 6, Fig. 7 shows the combination of the thicknesses of the InGaAs/GaAsSb layers with a cutoff wavelength of 2.37 μm at an operating temperature of 300 K.

In addition, as mentioned in Sect. 2.2, the greater the overlap between the wave functions of electrons and holes, the greater the probability of optical transition between semiconductors, which leads to an improvement in quantum efficiency. Figure 8 shows a plot of the T2SL structural parameters that satisfy the cutoff wavelength for the simulation results of the amount of wave function overlap. From Fig. 8, InGaAs:5 nm/GaAsSb:3 nm, which satisfies the desired cutoff wavelength and maximizes the amount of wave function overlap, was selected as the T2SL structural parameter.

2.5　Absorption layer thickness of experimental sample

The total thickness of the absorption layer can be adjusted by increasing or decreasing the number of pairs of InGaAs/GaAsSb layers that constitute the absorption layer. Theoretically, as the absorption layer becomes thicker, the absorption efficiency of incident light and the quantum
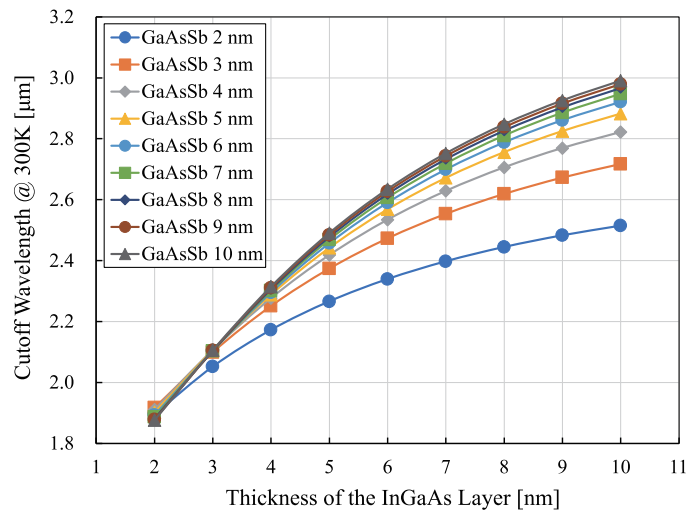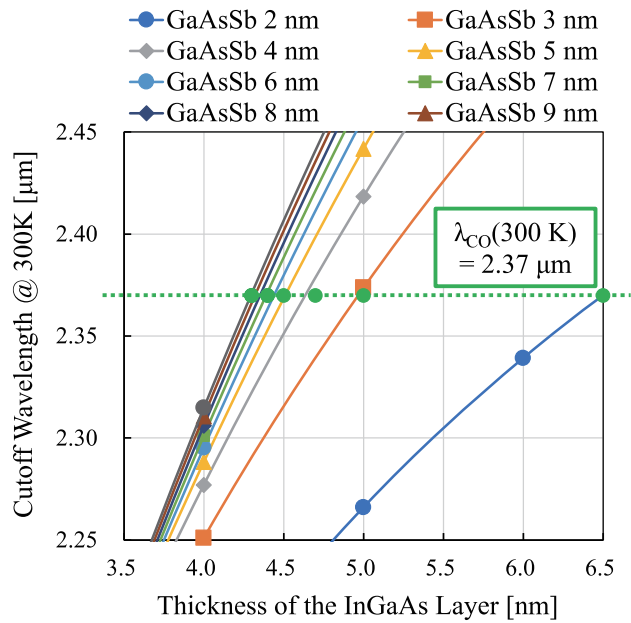
Fig. 6.   (Color online) Simulation results of the relationship between the thicknesses of the InGaAs/GaAsSb layers and the cutoff wavelength at 300 K.

InGaAs layer Thickness [nm]	GaAsSb layer Thickness [nm]
6.5	2.0
5.0	3.0
4.7	4.0
4.5	5.0
4.4	6.0
4.4	7.0
4.3	8.0
4.3	9.0
4.3	10.0

Combination of the layer thicknesses that satisfy $\lambda_{CO}(300K) = 2.37 \mu m$

Fig. 7.   (Color online) T2SL structure parameters that satisfy the cutoff wavelength condition.
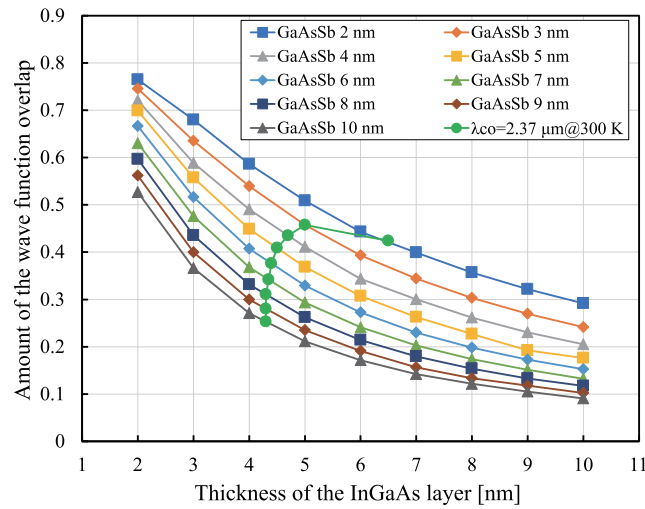
Fig. 8.   (Color online) T2SL structural parameters that maximize the amount of wave function overlap.

efficiency improve. The relationship between the total thickness of the absorption layer and the quantum efficiency is expressed by

$$\eta \propto 1 - e^{-ad} \quad . \tag{10}$$

Here, d is the total thickness of the absorption layer, η is the quantum efficiency, and a is the absorption coefficient of the absorption layer. As the thickness of the absorption layer increases, the dark current density also increases.[12] However, we do not have reliable data that clearly show the relationship among the total thickness of the absorption layer, the dark current density, and the quantum efficiency. Therefore, we decided to fabricate an experimental sample and examined the appropriate thickness of the absorption layer.

Furthermore, since both quantum efficiency and dark current density increase with the thickness of the absorption layer, trends in photodetector performance can be confirmed by examining three absorption layer thicknesses. First, we selected 2.5 μm (310 pairs), which has a proven track record of being used in consumer products. However, in this case, there was concern that the sensitivity of the photodetector seems to be insufficient for the purpose of this study. In addition, in the consumer field, an absorption layer thickness of 4.5 μm has been evaluated to improve sensitivity. However, the crystallinity deteriorated and the dark current density became extremely large. Therefore, we selected 4.0 μm as a challenging value to improve quantum efficiency. Finally, we selected 3.2 μm, which is an intermediate value between 2.5 and 4.0 μm.

3.   Measurement by Experimental Sample

3.1   T2SL single-pixel pin-photodiode fabrication

Figure 9 shows the structure of a T2SL single-pixel pin-photodiode experimental sample. We have grown an epitaxial wafer on an InP substrate by metal organic chemical vapor deposition. Also, as mentioned in Sect. 2.2, we selected InP as the crystal growth substrate owing to its various advantages. Three types of T2SL single-pixel pin-photodiode sample were fabricated on the basis of the thickness of the absorption layer described in Sect. 2.4.

3.2   Measurement results of dark current density

Figure 10 shows the measurement results of the dark current density. InGaAs/GaAsSb photodiodes have four types of dark current. They are generated recombination (G-R) current, direct tunnel current, trap-assisted tunnel current, and diffusion current.[13,14] The G-R current occurs even when the detector is under normal condition. However, if the bias voltage is very large, the direct tunnel current occurs. Also, if there are many impurities and lattice defects in the crystal, the trap-assisted tunnel current increases. The diffusion current occurs when the operating temperature of the detector is as high as 60 ℃; thus, the diffusion current is beyond the scope of this study. If these dark currents are plotted on a graph with the horizontal axis as the bias voltage and the vertical axis as the dark current, the type of dark current can be estimated since the G-R current is almost a horizontal line and the other dark currents are diagonal lines.

From Fig. 10, the main component of the dark current is the G-R current, which is considered to be caused by the thermal excitation of carriers in the depletion layer. Furthermore, since there is almost no direct or trap-assisted tunnel current, it is considered that the crystal growth of the pin-photodiode was performed appropriately. In addition, it can be seen that the dark current
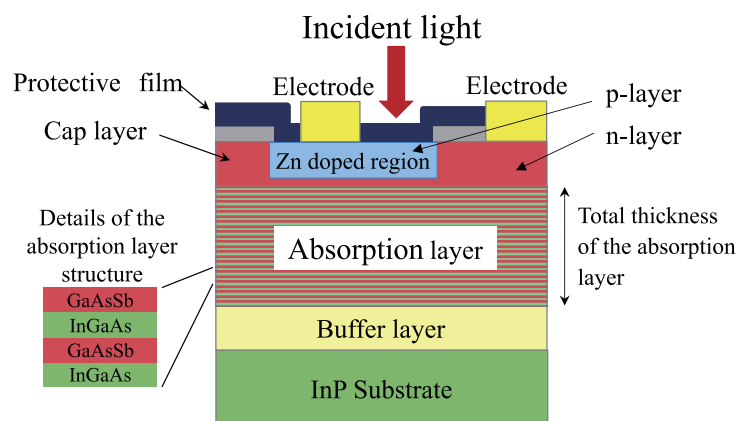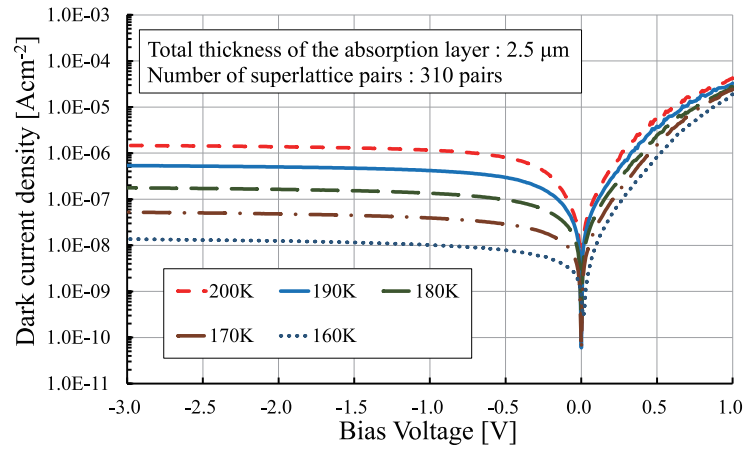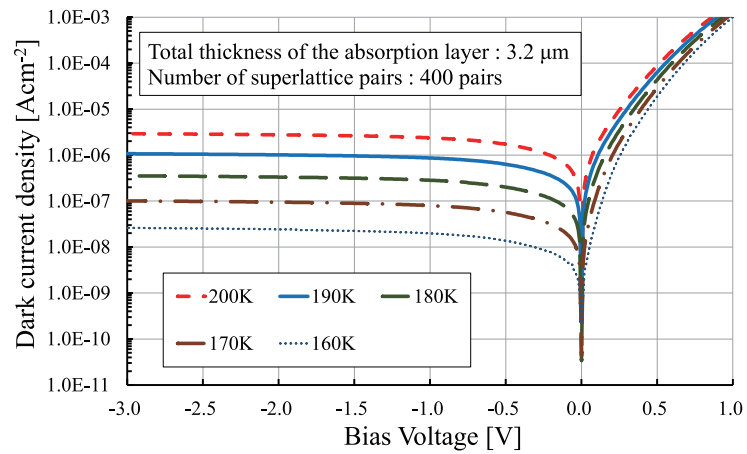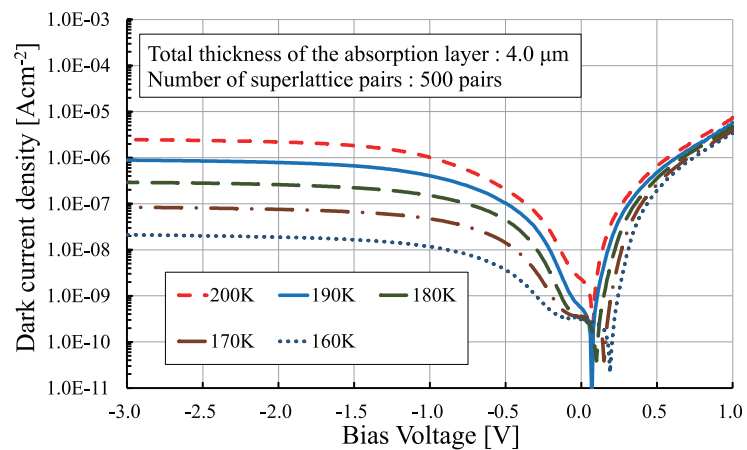

Fig. 9.   (Color online) Structure of the T2SL single-pixel pin-photodiode experimental sample.

(a)

(b)

(c)

Fig. 10.   (Color online) Measurement result of the dark current density of the T2SL single-pixel pin-photodiode experimental sample. Total thickness of the absorption layer: (a) 2.5 μm, (b) 3.2 μm, and (c) 4.0 μm.

density increases with the operating temperature of the experimental sample. This is because when the main component of the dark current is the G-R current, the rates of carrier generation and recombination in the depletion layer increase with the operating temperature.

It was also expected that increasing the total thickness of the absorption layer would cause the deterioration of the crystallinity and increase the dark current. However, from the results, no notable increase in dark current was observed. A possible reason for this is that T2SL is a simple repeating structure of thin layers, and there was no significant deterioration in crystallinity within the parameters.

3.3 Measurement results of spectral sensitivity

Figure 11 shows the measurement results of the spectral sensitivity. First, focusing on the bias voltage, it can be seen that when the bias voltage is large, there is a constant sensitivity around the 2.2 μm band regardless of the operating temperature and total thickness of the absorption layer. The reason for this is considered to be that when the bias voltage is large, the energy band is tilted and the number of transitions from high quantum levels increases. In addition, a large bias voltage contributes to the transport ability of carriers excited by incident infrared radiation.[15] Therefore, a larger bias voltage is desirable in this study.

Next, concerning the operating temperature, the sensitivity around the 2.2 μm band is higher when the operating temperature is high than when it is low. The reason for this is considered to be that when the operating temperature is high, the thermal energy of the carriers and the number of transitions from high quantum levels increase.[15]
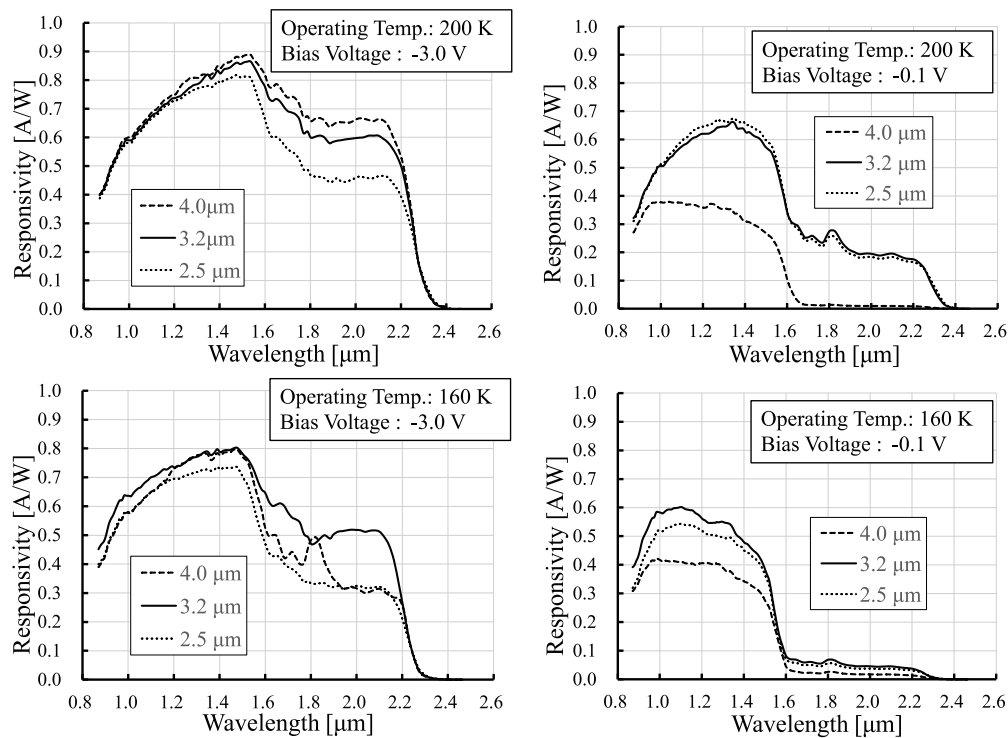
Fig. 11. Measurement results of the spectral sensitivity.

3.4   Evaluation of T2SL focal plane array (FPA) experimental sample

Figure 12 shows the cross-sectional structure of the T2SL FPA experimental sample. A pin-photodiode superlattice array stacked on an InP substrate is connected to a readout integrated circuit with indium bumps. Infrared rays enter from the InP substrate side. It also has a planar structure in which a photodiode is formed on a crystal grown on an InP substrate by diffusion. This method has been proven as a manufacturing technology for communication photodiodes with InGaAs grown on an InP substrate. On the other hand, as another device structure, there is a mesa structure in which pixels are separated by etching. This structure has advantages such as being able to suppress crosstalk with adjacent pixels. However, in the case of the mesa structure, the side surface of the pixel is damaged by etching. Thus, an advanced manufacturing technology is required to treat the damaged part of the side surface of the pixel and to protect it with an insulating layer. Therefore, we selected a highly reliable planar structure.

Figure 13 shows the measurement results of the quantum efficiency of the T2SL FPA experimental sample. We finally set the absorption layer thickness of the SWIR T2SL photodetector to 3.2 μm and the bias voltage to −3.0 V. Moreover, after comprehensively considering the performance of the T2SL photodetector to utilize night airglow, we set the operating temperature to 160 K. Then, we confirmed that this SWIR T2SL photodetector has sufficient quantum efficiency in the desired wavelength band. Finally, Fig. 14 shows an image obtained by the SWIR T2SL photodetector that we developed in this study.
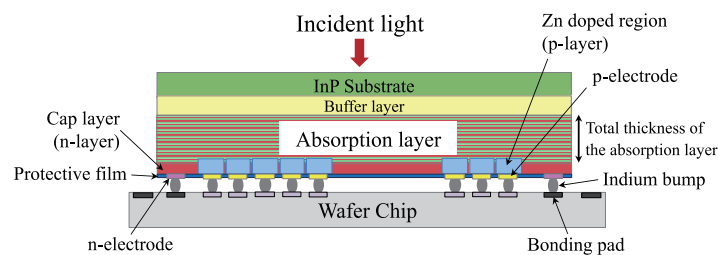

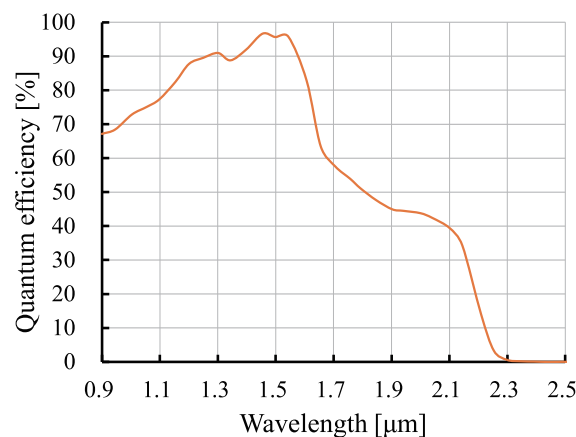Fig. 12.   (Color online) Cross-sectional structure of the T2SL focal plane array.

Fig. 13.   (Color online) Quantum efficiency of the T2SL focal plane array (total thickness of the absorption layer: 3.2 μm, bias voltage: −3.0 V, operating temperature: 160 K).

Fig. 14.   Image obtained by the T2SL FPA experimental sample in this study.

4.   Conclusion

In this paper, we summarize the results of the development of the InGaAs/GaAsSb T2SL photodetector that can utilize night airglow. We performed T2SL structural simulations and found a combination of InGaAs/GaAsSb layer thicknesses, which satisfies the desired detection wavelength band and is considered to have the highest sensitivity. On the basis of the simulation results, we fabricated three types of T2SL single-pixel pin-photodiode experimental sample with different absorption layer thicknesses. We aimed to improve the sensor performance by increasing the total thickness of the absorption layer. However, although the crystal growth was considered to have been performed sufficiently, the sensor performance could not be improved as expected. Also, we fabricated FPA to confirm that it had appropriate sensitivity in the desired wavelength band, and we were able to obtain a clear image. We believe that this paper can contribute to the further development of the T2SL photodetector. From now on, we would like to analyze data from field tests and work on low-noise signal readout.

References

1   H. Ishikawa, T. Takahashi, F. Mizuno, T. Suzuki, E. Yamada, Y. Ozaki, and D. Ishikawa: SEI Technical Reciew. **182** (2013) (in Japanese). https://sumitomoelectric.com/jp/sites/japan/files/2021-07/download_documents/sei10757.pdf

2   H. Inada, H. Mori, Y. Nagai, Y. Iguchi, T. Saitoh, K. Fujii, T. Ishizuka, and K. Akita: Proc. SPIE **8012** (2011) 801220. https://doi.org/10.1117/12.888096

3   R. Sidhu, N. Duan, J. C. Campbell, and A. L. Holmes: IEEE Photonics Technol. Lett. **17** (2005) 2715. https://doi.org/10.1109/LPT.2005.859163

4   D. C. Dayton, J. Allen, R. Nolasco, J. D. Gonglewski, M. Myers, D. Burns, I. Mons, and F. Maia: Proc. SPIE **8014** (2011) 801407. https://doi.org/10.1117/12.884233

5   Ch. Leinert, S. Bowyer, L. K. Haikala, M. S. Hanner, M. G. Hauser, A.-Ch. Levasseur-Regourd, I. Mann, K. Mattila, W. T. Reach, W. Schlosser, H. J. Staude, G. N. Toller, J. L. Weiland, J. L. Weinberg, and A. N. Witt: Astron. Astrophys. Suppl. Ser. **127** (1998) 1. https://doi.org/10.1051/aas:1998105

6   W. E. Tennant, J. M. Arias, and J. Bajaj: Proc. SPIE **7298** (2009) 72982V. https://doi.org/10.1117/12.821350

7 K. Miura: Doctoral Thesis at Osaka Prefecture University "A Study on Growth Technology of Novel Materials For Absorption Layers of Infrared Sensors by Molecular Beam Epitaxy Method on InP Substrates" (2013). https://doi.org/10.24729/00000081

8 K. Miura, Y. Iguchi, T. Katsuyama, and Y. Kawamura: SEI Technical Reciew. **184** (2014) (in Japanese). https://sumitomoelectric.com/technology/tr/bn184/pdf/sei10797.pdf

9 R. Pino, Y. Ko, and P. S. Dutta: J. Appl. Phys. **96** (2004) 1064. https://doi.org/10.1063/1.1738527

10 Y. P. Varshni: Physica **34** (1967) 149. https://doi.org/10.1016/0031-8914(67)90062-6

11 H. Tanoue: Doctoral Thesis at Tokyo Metropolitan University "Fabrication and evaluation of high-density InGaAs strained quantum dot laser using high-speed molecular beam epitaxy growth technology" (2013) (in Japanese).

12 L. Zheng, M. Tidrow, L. Aitcheson, J. O'Connor, and S. Brown: Proc. SPIE **7660** (2010) 76601E. https://doi.org/10.1117/12.852239

13 B. Chen, J. Yuan, and A. L. Holmes Jr: Opt Quantum Electron. **45** (2013) 271. https://doi.org/10.1007/s11082-012-9624-6

14 B. Chen, W. Jiang, J. Yuan, and A. L. Holmes Jr: IEEE J. Quantum Electron. **47** (2011) 1244 https://doi.org/10.1109/JQE.2011.2160450

15 H. Inada, K. Machinaga, S. Balasekaran, K. Miura, T. Kawahara, M. Migita, H. Obi, T. Fuyuki, K. Fujii, T. Ishizuka, and Y. Iguchi: Proc. SPIE **10177** (2017) 1017704. https://doi.org/10.1117/12.2262465